

# Ice Modeling Indicates Formation Mechanisms of Large-scale Folding in Greenland's Ice Sheet

Yu Zhang<sup>1</sup>, Till Sachau<sup>2</sup>, Steven Franke<sup>3</sup>, Haibin Yang<sup>4</sup>, Dian Li<sup>5</sup>, Ilka Weikusat<sup>6</sup>, and Paul D Bons<sup>7</sup>

<sup>1</sup>Tübingen University

<sup>2</sup>University of Tuebingen

<sup>3</sup>Department of Geosciences, Tübingen University

<sup>4</sup>Zhejiang University

<sup>5</sup>School of Earth Sciences, Chengdu University of Technology

<sup>6</sup>Alfred Wegener Institute

<sup>7</sup>Universität Tübingen

December 10, 2023

## Abstract

Radio-echo sounding (RES) has shown that large-scale folds in the englacial stratigraphy is ubiquitous in Greenland's ice sheet. However, there is no consensus yet on how these folds form. Here, we use the full-Stokes code Underworld2 to simulate ice movements in three-dimensional convergent flow, mainly investigating the effect of ice anisotropy due to a crystallographic preferred orientation, vertical viscosity and density contrasts in ice layers, and bedrock topography. Our simulated folds show complex patterns and are classified into three types: large-scale folds, small-scale folds and basal-shear folds. The amplitudes of large-scale folds tend to be at their maximum in middle ice layers and decrease towards the surface, in accordance with observations in RES data. We conclude that bedrock topography contributes to perturbations in ice layers, and that ice anisotropy amplifies these into large-scale folds, while vertical viscosity contrasts in ice layers are insufficient for large-scale fold amplification.

## Hosted file

981530\_0\_art\_file\_11665096\_s59n7v.docx available at <https://authorea.com/users/707174/articles/692216-ice-modeling-indicates-formation-mechanisms-of-large-scale-folding-in-greenland-s-ice-sheet>

## Hosted file

981530\_0\_supp\_11663706\_s5920f.docx available at <https://authorea.com/users/707174/articles/692216-ice-modeling-indicates-formation-mechanisms-of-large-scale-folding-in-greenland-s-ice-sheet>

1  
2 **Ice Modeling Indicates Formation Mechanisms of Large-scale Folding in**  
3 **Greenland's Ice Sheet**

4 **Yu Zhang<sup>1</sup>, Till Sachau<sup>1</sup>, Steven Franke<sup>1,2</sup>, Haibin Yang<sup>3</sup>, Dian Li<sup>1,4</sup>, Ilka Weikusat<sup>1,2</sup>, and**  
5 **Paul D. Bons<sup>1,5</sup>**

6 <sup>1</sup>Department of Geosciences, Tübingen University, Tübingen, Germany.

7 <sup>2</sup>Alfred Wegener Institute, Helmholtz Centre for Polar and Marine Research, Bremerhaven,  
8 Germany.

9 <sup>3</sup>School of Earth Sciences, Zhejiang University, Hangzhou, China.

10 <sup>4</sup>College of Earth Science, Chengdu University of Technology, Chengdu, China.

11 <sup>5</sup>School of Earth Science and Resources, China University of Geosciences (Beijing), Beijing,  
12 China.

13 Corresponding author: Y. Zhang ([yu.zhang@mnf.uni-tuebingen.de](mailto:yu.zhang@mnf.uni-tuebingen.de)), P. D. Bons ([paul.bons@uni-](mailto:paul.bons@uni-tuebingen.de)  
14 [tuebingen.de](mailto:paul.bons@uni-tuebingen.de))

15 **Key Points:**

- 16 • The formation of large-scale folds in polar ice sheets is controlled by ice anisotropy and  
17 bedrock topography
- 18 • Ice anisotropy can also produce small-scale folds of originally flat ice layers
- 19 • The implementation of ice anisotropy should be included in large-scale ice flow modeling

## 20 **Abstract**

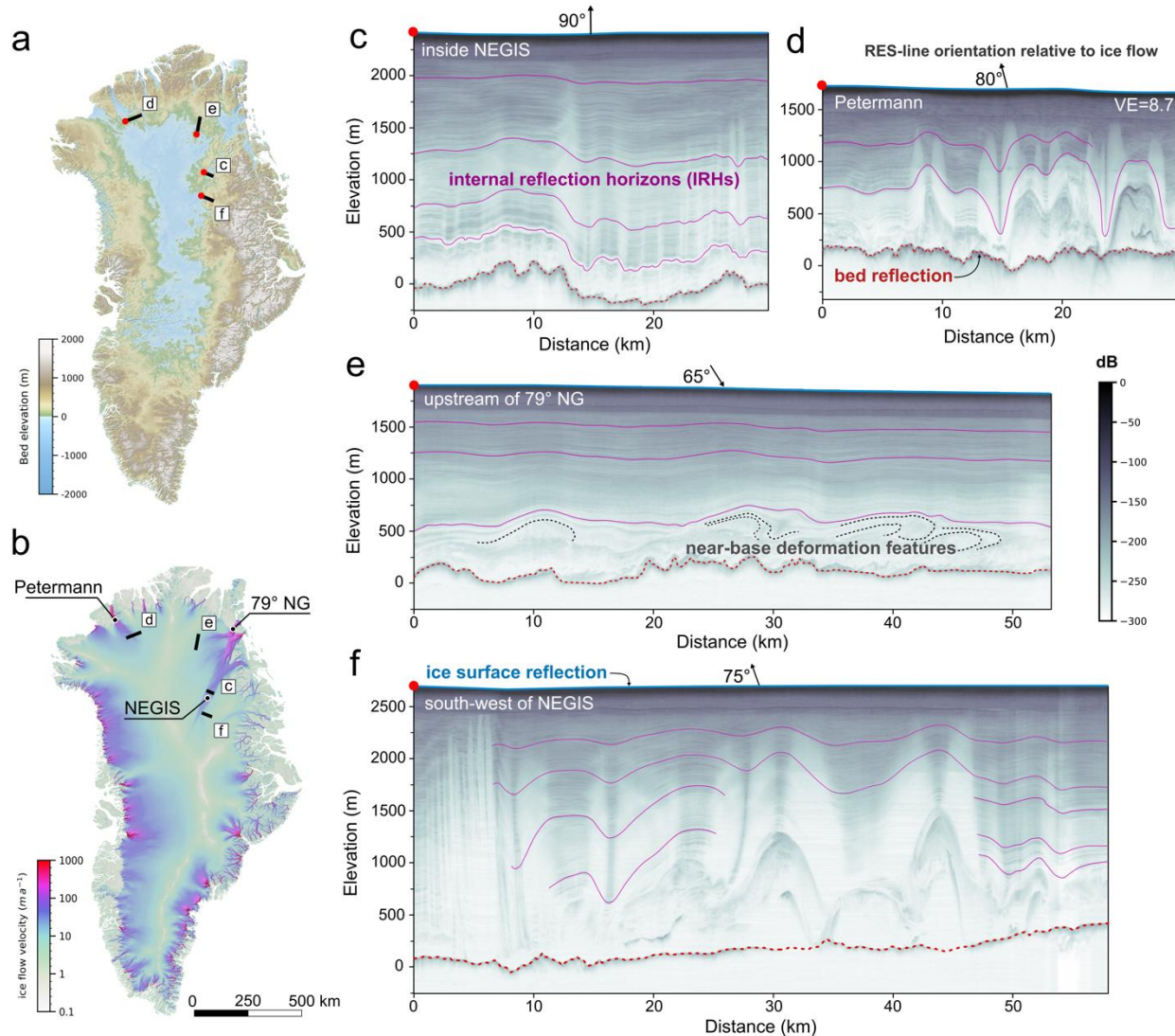
21 Radio-echo sounding (RES) has shown that large-scale folds in the englacial stratigraphy is  
22 ubiquitous in Greenland's ice sheet. However, there is no consensus yet on how these folds form.  
23 Here, we use the full-Stokes code Underworld2 to simulate ice movements in three-dimensional  
24 convergent flow, mainly investigating the effect of ice anisotropy due to a crystallographic  
25 preferred orientation, vertical viscosity and density contrasts in ice layers, and bedrock  
26 topography. Our simulated folds show complex patterns and are classified into three types: large-  
27 scale folds, small-scale folds and basal-shear folds. The amplitudes of large-scale folds tend to  
28 be at their maximum in middle ice layers and decrease towards the surface, in accordance with  
29 observations in RES data. We conclude that bedrock topography contributes to perturbations in  
30 ice layers, and that ice anisotropy amplifies these into large-scale folds, while vertical viscosity  
31 contrasts in ice layers are insufficient for large-scale fold amplification.

## 32 **Plain Language Summary**

33 Polar ice sheets are composed of compacted former snow layers that have been deposited at the  
34 ice surface. If not distorted or deformed, these layers are flat or adapt to the underlying bed  
35 topography. However, vertical radar scans of the Greenland ice sheet show large-scale folds of  
36 up to hundreds of meters in height. To investigate how these large-scale folds form, we set up a  
37 three-dimensional numerical ice-sheet model and simulate fold growth. Our modeling  
38 emphasizes the distinctive physical properties of ice required for fold formation, notably its  
39 anisotropy (the direction dependency of the flow strength) and power-law rheology (when ice  
40 becomes softer with increasing strain rate). These findings may introduce novel perspectives to  
41 the glaciological community regarding the dynamics of ice flow. For instance, the power-law  
42 behavior of ice could potentially be influenced by anisotropy and bottom shearing during flow.  
43 This suggests that ice sheets might exhibit increased instability when set in motion, raising  
44 important concerns within the field of glaciology.

## 45 **1 Introduction**

46 Airborne radio-echo sounding (RES) data reveal internal layering and large-scale folding  
47 (up to > 100 m fold amplitude) on the bumpy bedrock in several regions of the Greenland Ice  
48 Sheet (GrIS, Figure 1) (Bell et al., 2014; Bons et al., 2016; Franke et al., 2022a, 2022b;  
49 Leysinger-Vieli et al., 2018; MacGregor et al., 2015; NEEM community members, 2013;  
50 Wolovick et al., 2014). The large-scale folds appear both within ice streams and in regions of  
51 slow-moving ice. Fold amplitudes usually reach their maximum in the middle layers, gradually  
52 decrease towards upper layers and flatten at the ice surface. These folds play a significant role in  
53 the interpretation of the stratigraphy in ice cores (NEEM community members, 2013), the past  
54 and present ice flow dynamics (Franke et al., 2022a), and basal conditions (Leysinger-Vieli et  
55 al., 2018; Wolovick et al., 2014).



56  
 57 **Figure 1.** Overview of the Greenland ice sheet and radio-echo sounding (RES) profiles: (a) bed  
 58 topography (Morlighem et al., 2017) and location of RES profiles; (b) ice surface flow velocity  
 59 (Joughin et al., 2018); (c-f) RES images showing englacial folds (c) in the central North-East  
 60 Greenland Ice Stream (NEGIS), (d) at the Petermann ice stream, (e) upstream of the 79° North  
 61 Glacier (Nioghalvfjærdsbrae), and (f) in the upstream region of the NEGIS. Note the strong  
 62 vertical exaggeration (8.7) in RES-profiles. Arrows show the average flow direction relative to  
 63 the profiles.  
 64

65 Several mechanisms and models have been proposed to explain the formation of folds in  
 66 the ice sheet. Bell et al. (2014) and Leysinger-Vieli et al. (2018) suggest that refreezing  
 67 meltwater adds material to the ice base and elevates the overlying stratigraphy and influences  
 68 basal ice deformation. Alternatively, Wolovick et al. (2014) suggest that variable slip rates due to  
 69 “basal slippery patches” can create large-scale folds. Furthermore, Krabbendam (2016) proposes  
 70 the basal temperate (melting) ice layer may be locally thickened by internal deformation of  
 71 folding or thrusting over a bedrock high. The above mentioned variable basal resistance or basal  
 72 freeze-on/melting models all require special or complex basal ice and bedrock conditions, which

73 seems at odds with the presence of folds throughout the GrIS. Additionally, all these concepts  
74 use single RES sections and implicitly assume that the fold axis orientation is at a high angle to  
75 the direction of ice flow. However, the three-dimensional geometry of folds show that folds are  
76 rather parallel or at a small angle to the flow direction (Bons et al., 2016; Franke et al., 2022a,  
77 2023).

78 Hudleston (2015) proposes that irregularities in primary ice stratification can be  
79 kinematically amplified in convergent flow by horizontal shortening and without the requirement  
80 of rheological contrast in the ice. Bons et al. (2016) suggest that mechanical anisotropy and  
81 convergent flow cause large-scale folding in Greenland's ice sheet. However, the question which  
82 factors actually contribute to folding, or why initial irregularities of ice layers would be  
83 amplified, is still unclear. Moreover, there is a need for more and better numerical modeling to  
84 trace the widespread deformation of internal ice layers.

85 Three properties of ice or ice sheets are significant for the modeling of flow in ice sheets:  
86 (1) The viscoplastic deformation of the ice  $I_h$  (hexagonal ice) results essentially from dislocation  
87 glide parallel to the crystallographic basal plane (Gillet-Chaulet et al., 2006). The  
88 crystallographic preferred orientation (CPO) in ice sheets is typically a vertical alignment of the  
89 crystals' c-axes, which are perpendicular to the easy-glide basal planes. As a result, the ice  
90 becomes significantly anisotropic in its flow properties (Duval et al., 1983; Llorens et al., 2017).  
91 (2) Due to geothermal heat flux (Artemieva, 2019), ice temperature increases with depth: upper  
92 "cold ice" has a high viscosity and density, while the lower "warm ice" has a lower viscosity and  
93 also has a low density due to thermal expansion (Hills et al., 2017; Krabbendam, 2016). (3) Ice  
94 layers are initially not necessarily perfect sheets with constant thickness, and variations in  
95 thickness may form due to the underlying bedrock topography (Hudleston, 2015). Taking these  
96 considerations into account, we here use numerical modeling to investigate the development of  
97 folds in 3D convergent flow. We particularly investigate the factors of rheological anisotropy of  
98 ice, vertical viscosity and density contrasts, and bedrock conditions.

## 99 **2 Method**

### 100 **2.1 Full-Stokes Code Underworld2**

101 We used the Full-Stokes software "Underworld 2" (Beucher et al., 2022). The code was  
102 originally designed and developed for modeling and tracking internal deformation in  
103 geodynamic processes and is therefore specifically optimized for our case. Some of the  
104 advantages are (i) tracking of material "particles" during deformation and (ii) local fabric  
105 evolution can be coupled to the local rheological anisotropy.

106 Underworld 2 uses the material point method (MPM), which is related to the better-  
107 known particle-in-cell method (Moresi et al., 2003). MPM uses an Eulerian finite-element mesh  
108 to calculate the incremental development of the velocity field and other field variables, such as  
109 temperature and pressure, while Lagrangian material points ("particles") carry the density,  
110 viscosity, lattice orientation, and other relevant local material parameters. This code is already  
111 well established in complex geodynamic modeling with a full-Stokes solution for isotropic and  
112 anisotropic elasto-visco-plastic materials (Moresi & Mühlhaus, 2006; Sharples et al., 2016). The  
113 software has also passed the usual benchmark tests for full-Stokes ice sheet models of Pattyn et  
114 al. (2008) (Sachau et al., 2022).

## 115 2.2 Physics

116 In our model, the temperature ( $T$ , °C) is  $-30$  °C ( $T_0$ ) for cold ice and, below a height  
 117  $h_{\text{warmice}}$ , in what is here termed "warm ice", the temperature increases downward to  $-3$  °C ( $T_{\text{bed}}$ ) at  
 118 the base (Hills et al., 2017; Rogozhina et al., 2011) with a parabolic equation:

$$119 \quad T = T_{\text{bed}} + (T_0 - T_{\text{bed}}) \left( \frac{y - h_{\text{bed}}}{h_{\text{warmice}} - h_{\text{bed}}} \right)^{1.2} \quad (1)$$

120 where  $y$  is the height in warm ice, and  $h_{\text{bed}}$  and  $h_{\text{warmice}}$  are the heights for bedrock surface and  
 121 warm ice surface.

122 The ice density ( $\rho$ , kg/m<sup>3</sup>) is given as a function of temperature by:

$$123 \quad \rho = \frac{1.802 \times 10^4}{19.30447 - 7.988471 \times 10^{-4} \cdot (T + 273) + 7.563261 \times 10^{-6} \cdot (T + 273)^2} \quad (2)$$

124 Equation (2) is derived from the molar volume equation for pure ice at 1 atm in Marion and  
 125 Jakubowski (2004), where the molar mass of H<sub>2</sub>O is assumed to be  $1.802 \times 10^4$  kg/mol.

126 The non-linear viscous ice flow is based on Kuiper's flow law for dislocation creep  
 127 (Kuiper et al., 2020), an advanced version from Glen (1955) and Goldsby (2006), where the  
 128 strain rate ( $\dot{\epsilon}_{ij}$ ) is proportional to the deviatoric stress ( $\tau_{ij}$ ) to the power  $n$ ,

$$129 \quad \dot{\epsilon}_{ij} = A_0 e^{\frac{-Q}{R(T+273)}} \tau_{II}^{n-1} \tau_{ij} \quad (3)$$

130 where  $A_0$  is the material parameter,  $Q$  the activation energy,  $R$  the gas constant and  $\tau_{II}$  the  
 131 second invariant of the deviatoric stress tensor  $\tau_{ij}$ , and the stress exponent  $n$  is 4 for polar ice  
 132 sheets (Bons et al., 2018). The power-law viscosity of ice (isotropic viscosity  $\eta_1$ , Pa · s) is  
 133 derived from temperature and strain rate (Sachau et al., 2022)

$$134 \quad \eta_1 = \frac{1}{2} \left( A_0 e^{\frac{-Q}{R(T+273)}} \right)^{\frac{-1}{n}} \cdot \dot{\epsilon}_{II}^{\frac{1-n}{n}} \cdot 10^6 \quad (4)$$

135 where  $\dot{\epsilon}_{II}$  is the second invariant of the strain rate tensor.

136 The c-axis orientation of the ice crystal is stored for each particle in Underworld2. Initial  
 137 c-axis directions of ice particles are perpendicular to the local layer orientation with a Gaussian  
 138 random distribution with a standard deviation of  $\pm 5^\circ$ . As the simulation progresses, the c-axes  
 139 rotate in the flow field according to the symmetric deformation-rate tensor  $D$  and the skew-  
 140 symmetric rotation-rate tensor  $W$

$$141 \quad D = \frac{1}{2} (L + L^T) \quad (5)$$

$$142 \quad W = \frac{1}{2} (L - L^T) \quad (6)$$

143 where  $L$  is the velocity gradient tensor (see Appendix B in Sharples et al. (2016) for detailed  
 144 rotation equations).

145 The anisotropy of the ice crystal is modeled as transverse isotropy, which is a common  
 146 practice in numerical modeling (Gillet-Chaulet et al., 2005; Martín et al., 2009; Sharples et al.,  
 147 2016). Transverse isotropic viscosity is defined by two viscosity values: a general viscosity  $\eta_1$   
 148 (Pa · s) and a second viscosity  $\eta_2$  (Pa · s) perpendicular to the c-axis direction.  $\eta_1$  is set  
 149 proportional to  $\eta_2$ :

$$150 \quad \eta_1 = k\eta_2 \quad (7)$$

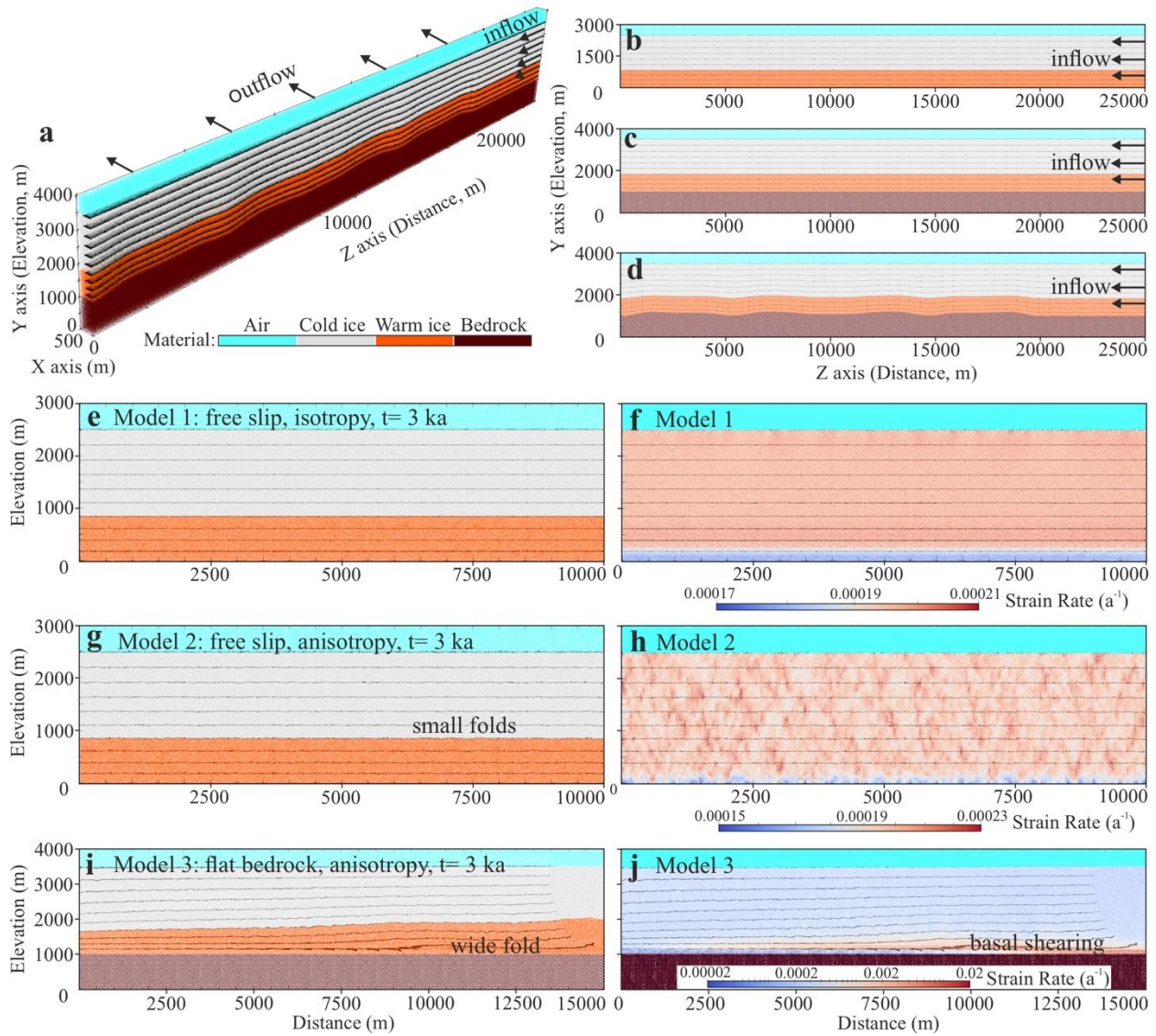
151 where  $k$  represents the rheological anisotropy value. If the stress exponent  $n$  is 3 and given the  
 152 same strain rate, the stress required for non-basal deformation of ice monocrystals is at least 60  
 153 times higher than for basal slip (Llorens et al., 2017). For macroscopic ice polycrystals, the ratio  
 154 is about ten (Duval et al., 1983). For the assumed  $n = 4$  in our macroscopic ice model,  $k$  is  
 155 approximately six. However,  $k = 6$  requires a high grid resolution to avoid numerical instabilities  
 156 that may lead to artificial amplification of small folds. For this reason we employed a smaller  $k =$   
 157 3, which thus underestimates the expected anisotropy in the ice. We will show that the main  
 158 factor controlling folding is not the  $k$ -value once significantly larger than unity, but whether the  
 159 ice is anisotropic or not.

### 160 2.3 Model Design

161 The basic design is shown in Figures 2a-2d (detailed parameters in Table S1 and Figure  
 162 S1 in Supporting Information SI). It consists of four main sets of layers: air (500 m), cold ice  
 163 (1667 m), warm ice (833 m) and bedrock, and 10 internal marker horizons to track the  
 164 deformation. Three different bedrock conditions are tested: (i) free-slip bottom boundary without  
 165 a bedrock (Figure 2b), (ii) a 1000 m thick bedrock layer with a flat surface to which the ice is  
 166 frozen (Figure 2c), and (iii) the same as (ii), but with an undulating bedrock surface with bumps  
 167 of variable wavelengths and amplitudes (Figure 2d). Internal horizons adapt to bedrock bumps,  
 168 where basal ice layers have larger initial amplitudes, which we refer to as 'noise' in this article.  
 169 The 'initial noise' gradually decreases from the ice-bedrock interface to zero at the ice surface.  
 170 Internal horizons are progressively shortened from the right (negative Z-axis direction) by a  
 171 lateral inflow at 5 m/yr, at the right boundary. The horizontal velocity is set to zero at the left  
 172 boundary. To reduce computing time, the model thus consist of one half of a convergent zone, as  
 173 for example envisaged by Bons et al. (2016) for the inlet area of the Petermann Glacier.  
 174 Simultaneously, there is outflow in the third dimension (positive X-axis; Figure 2a), which  
 175 compensates the inflow and thus maintains a constant ice volume.

176 Six models are discussed here for the impact of ice properties (anisotropy, viscosity and  
 177 density) and bedrock conditions on large-scale folding. In these models we varied the following  
 178 parameters: (1) bedrock condition (i) for Models 1-2, bedrock condition (ii) for Model 3, and  
 179 bedrock condition (iii) (variable amplitude bumps up to 400 m) for Models 4-5; (2) isotropic ice  
 180 for Model 1 and Model 5, and anisotropic ice for all other models (see detailed comparison of all  
 181 models in Table S2 in Supporting Information SI).

182



183  
 184 **Figure 2.** Model design and snapshots of results from Models 1-3 after 3000 years: (a) 3D view  
 185 of initial model (example from bumpy bedrock model); (b-d) profiles parallel to Z-Y coordinate  
 186 plane showing three bedrock types (b) free-slip bottom boundary, (c) flat bedrock surface and (d)  
 187 bumpy bedrock surface; (e-l) results of material map and the second invariant of strain-rate  
 188 magnitude for (e-f) Model 1, (g-h) Model 2 and (i-j) Model 3.  
 189

## 190 3 Results

### 191 3.1 Effect of Anisotropy, Viscosity and Density

192 In the simulations of isotropic ice on a free-slip bottom boundary (Model 1), ice layers  
 193 stay nearly flat for at least 3000 years, even with both vertical viscosity and density contrasts  
 194 (Figures 2e-2f). Nevertheless, when anisotropy is included in the models, a large number of  
 195 small folds (less than 40 m fold amplitude) form (Model 2; Figures 2g-2h), due to the Gaussian  
 196 variability of the c-axis orientation of particles. Compared to the very homogeneous strain rates

197 resulting from the isotropic Model 1 (Figure 2f), the strain-rate map of Model 2 is much more  
198 heterogeneous with clusters of high strain rates (Figure 2h).

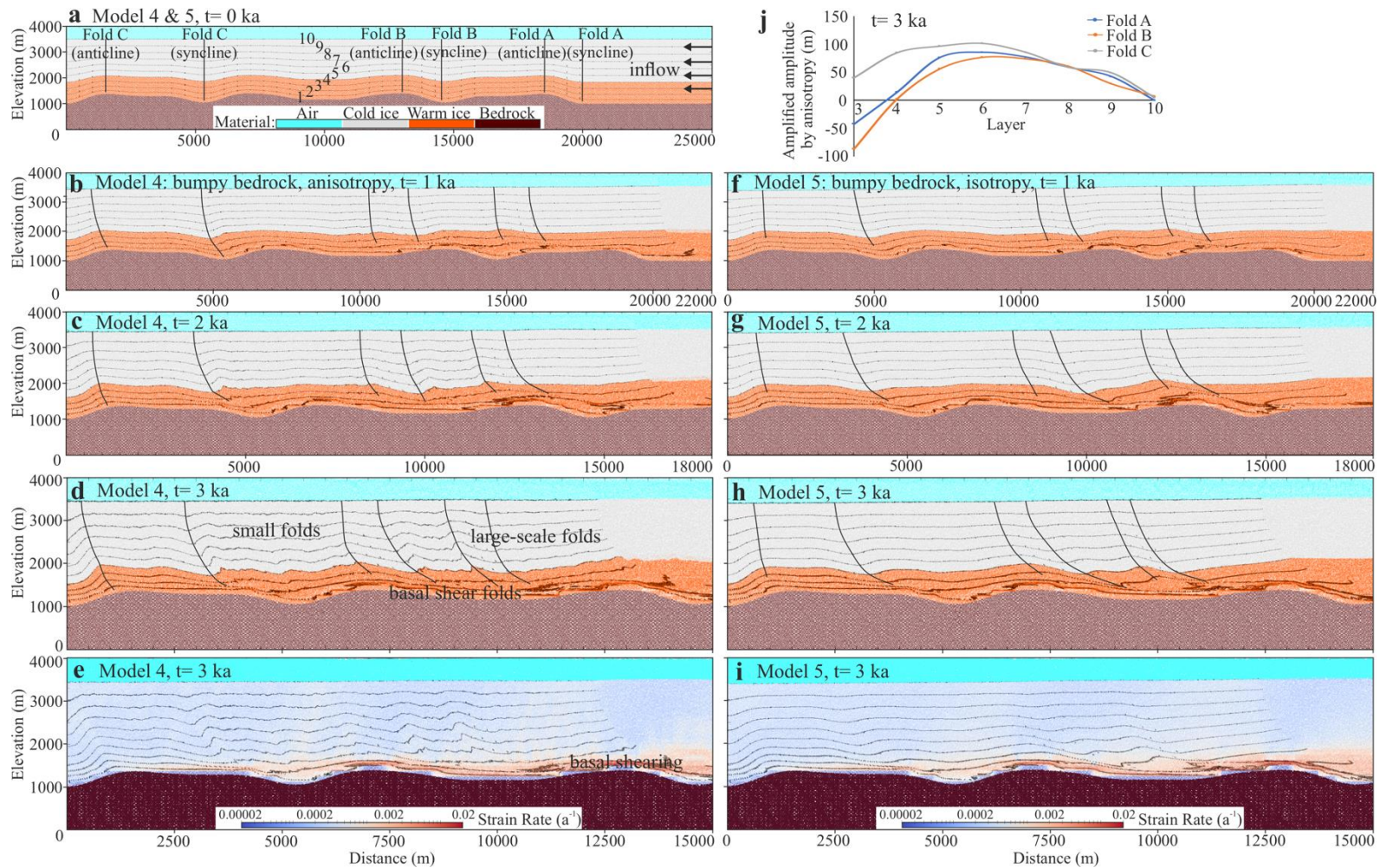
### 199 3.2 Effect of Bedrock Topography

200 In the scenario where bedrock is added as a horizontal flat layer underneath the  
201 anisotropic ice (Model 3; Figure 2i) shearing occurs to the basal ice layers as the ice is frozen to  
202 the bedrock. The slip resistance at the bedrock interface results in thickening of the ice at the  
203 inflow side, which shows as the development of a wide fold (up to 140 m amplitude). Abundant  
204 small folds appear with amplitudes that range up to 80 m around this wide fold. The strain-rate  
205 field (Figure 2j) shows a horizontal band of high strain rates along this wide fold. Strain rates  
206 decrease in upper ice layers but are still higher than in Model 2. For the scenario with a bumpy  
207 bedrock topography (Model 4), the initial ice layers on bedrock bumps start to evolve into large-  
208 scale folds (larger than 200 m amplitude after 3000 years) and additional small folds in between  
209 (Figures 3a-3e).

### 210 3.3 Anisotropic vs. isotropic ice on the bumpy bedrock

211 We explore the effect of anisotropic (Model 4) and isotropic ice (Model 5) on a bumpy  
212 bedrock in a 3000-year-long simulation (Figure 3). Here we compare three large-scale fold sets  
213 A, B, and C (Figure 3), in terms of the fold amplitudes as a function of layer height. Amplitude is  
214 here defined as the difference in elevation of a marker horizon at a fold crest and adjacent trough.  
215 The height is defined as the average of crest and trough elevation. We consider 10 stratigraphic  
216 layers labeled 1-10 from bottom to top (Figure 3a). The amplitude-height values of Layers 3-10  
217 are shown in Figure S4 in Supporting Information SI (note that Layers 1-2 are too close to the  
218 bedrock and therefore strongly sheared). In Model 4, the amplitude of the initial layer noise is  
219 largest in the near-base layers and zero at the ice surface. The largest fold amplitudes are in  
220 middle layers (Layers 4-6) and mostly exceed the initial layer noise. In the isotropic Model 5 we  
221 observe large-scale folds that are inherited from the initial noise. They are smaller and smoother,  
222 and without small folds in between (Figures 3f-3i). Folds with the largest amplitudes are found in  
223 the deepest layers, and amplitudes of most folds are smaller than the initial noise. Strain rates in  
224 Model 5 are high close to the ice base, decrease towards the ice surface in the upper layers and  
225 are distributed in a regular pattern associated with bedrock bumps (Figure 3i).

226 The only difference in the settings between Model 4 and Model 5 is the anisotropy in the  
227 ice. Since the fold growth of fold sets A, B and C is greater in the anisotropy case, we define the  
228 "amplified amplitude by anisotropy" by subtracting the fold amplitude of the isotropy model  
229 (Model 5) from that of the anisotropy model (Model 4). After 3000 years (Figure 3j), the  
230 amplified amplitudes by anisotropy of most folded layers are larger than 0 m, indicating that  
231 anisotropy does amplify folds after this period. The maximum amplification of over 100 m is in  
232 the middle layers (Layers 5-7).



233

234 **Figure 3.** Snapshots of comparison of anisotropic Model 4 and isotropic Model 5 with an identical bedrock topography with 400 m  
 235 tall bumps in both models shown in (a): (b-d) Layer geometry snapshots of Model 4 after (b) 1000 years, (c) 2000 years and (d) 3000  
 236 years. (e) The second invariant of strain-rate magnitude in Model 4 at 3000 years. (f-h) Layer geometry snapshots of Model 5 after  
 237 1000, 2000 and 3000 years. (i) The second invariant of strain-rate magnitude for Model 5 after 3000 years. Note that the z-axis and y-  
 238 axis scales between the images of individual time steps. (j) Amplified amplitudes by anisotropy of Layers 3-10 on Fold A, Fold B and  
 239 Fold C after 3000 years.

## 240 **4 Discussion**

### 241 4.1 Controlling factors for fold growth

242 The folds observed in our modeling can be classified into three types: large-scale folds  
243 (fold amplitudes  $>100$  m), small-scale folds (fold amplitudes  $\ll 100$  m, wavelength  $\ll$  km) and  
244 basal shear folds (recumbent folds). The large-scale folds have wavelengths in the order of a km  
245 or more. Their axial planes have a listric shape, with steep dips near the ice surface that become  
246 shallower towards the bedrock. Our simulated large-scale folds (in particular those in Model 4)  
247 show strong similarity to those observed in Greenland's ice sheet by e.g., MacGregor et al.  
248 (2015), Bons et al. (2016) and Franke et al. (2022a) (Figure 1).

249 The main controlling factors for large-scale folds in our simulations are ice anisotropy  
250 and the initial geometry dictated by the underlying bedrock topography. Folds in isotropic ice  
251 ( $k=1$ ) (Figures 3f-3i) are essentially palimpsests of the underlying bedrock topography that are  
252 passively transported away from the underlying bumps. They do not amplify by themselves, but  
253 passively change their shape as they travel over bedrock bumps. In the anisotropic model with  
254  $k=3$  (Figures 3b-3e), we observed additional fold-shape modification and amplification. When  $k$   
255 is set to 6 (Figure S5 in Supporting Information SI) this effect is even stronger. This is a clear  
256 indication that the anisotropy plays a primary role in fold amplification. However, we also  
257 observe that fold amplitudes increase with increasing bedrock topography, as can be seen in  
258 Figures 3b-3e, and S6-S7 (in Supporting Information SI) with the highest bedrock topography  
259 amplitude of 600 m.

260 According to classical fold theory (Biot, 1957; Schmalholz and Mancktelow, 2016) folds  
261 form by the amplification of small perturbations in the folding layer. In case of folding of a  
262 strong layer in a softer matrix, a dominant wavelength will develop as a function of layer  
263 thickness (the characteristic length scale of the system) and the viscosity ratio of the layer and  
264 matrix. The dominant wavelength is the wavelength with the highest amplification rate. In case  
265 of a single, but anisotropic medium, a characteristic length scale is absent. As a consequence  
266 there is no dominant wavelength that amplifies the most, and folds of all wavelengths may form  
267 simultaneously, including small-scale folds (Figure 2g). Bedrock topography creates seed folds  
268 with significant amplitudes. With these, the system can "skip" the initial fold nucleation for folds  
269 with these wavelengths. Depending on the intensity of the anisotropy ( $k$ ) these folds will amplify.  
270 However, in case of anisotropy small-scale folds will also nucleate due to small-scale  
271 perturbations (here the random noise in  $c$ -axis orientations).

272 In our models, the lowermost ice is warmer, which creates a system with a cold and  
273 strong layer at the top and a warmer and softer layer at the bottom. At the top the cold ice is in  
274 contact with air, which has an almost infinitely lower viscosity compared to ice. Shortening of  
275 this layer system could potentially lead to buckle folding, as has been suggested by the NEEM-  
276 community (2013). Initial wavelengths for low viscosity contrasts would be at least five to ten  
277 times the layer thickness (Llorens et al., 2013; Schmalholz and Mancktelow, 2016), which in our  
278 case would be at least 5 to 10 km. However, the dominant wavelength due to the ice-air interface  
279 with an almost infinite viscosity contrast would by far exceed the width of the model, and even

280 that of an ice sheet. The viscosity contrast between the warm and cold ice is relatively low and  
281 lacks a sharp boundary. Although the resulting wavelengths are in the same order as of folds  
282 observed in the ice sheets, the amplification rate is very small (Llorens et al., 2013) and no  
283 visible folds can form. These theoretical considerations, as well as the results of models 1 and 3  
284 (isotropy, no bedrock bumps), indicate that Biot-type buckle folding due to viscosity contrasts  
285 between cold ice and air above and warm ice below cannot lead to significant folding on the  
286 multi-km scale.

287 Deformation in the deepest, softest ice is approximately in simple shear. In case of  
288 bedrock bumps, the basal shear zone may localise above the bedrock-ice interface, especially  
289 across throughs in the bedrock (Figure 3e). This effect is more pronounced in case of anisotropy  
290 (Sachau et al., 2022). Passive shearing of layers in heterogeneous simple shear leads to tight  
291 recumbent folds (Figures 3d and 3h) that are also observed in ice sheets (Figure 1e; Bons et al.,  
292 2016). Recumbent folding may be enhanced by anisotropy, but is largely controlled by the deep  
293 bedrock-parallel shearing and bedrock topography, not by anisotropy. Connection of the deep  
294 recumbent folds with a shallowly dipping axial plane with more upright folds higher up in the ice  
295 leads to the listric shape of the axial planes (Franke et al., 2022a).

#### 296 4.2 A generic mode for large-scale folding

297 Tracking the kinematic processes of ice layers, the formation of large-scale folding can  
298 be summarized in three stages: (1) Irregularities in primary ice stratification result mainly from  
299 undulating bedrock topography and become initial seeds for subsequent large-scale folding. (2)  
300 As lateral convergence continues, anisotropy comes into play and initial noise in the internal  
301 horizons is amplified. Internal ice horizons deform especially at both sides of a bedrock bump,  
302 but not on the summit of the bump where the ice above the basal shear zone can slide without  
303 further folding (Figure 3e). Meanwhile, anisotropy does also lead to smaller-scale folds that  
304 result from the amplification of noise in the system. The constraint of the bedrock has a  
305 significant impact on the deepest stratigraphic horizons, which can shear, rotate and develop  
306 complex structural patterns. (3) Finally, initial noise evolves into larger-scale folds and internal  
307 horizons in the middle of the ice column are amplified the most (not necessarily at the interface  
308 of warm and cold ice).

309 We should notice that our model may not yet well explain some extremely tall plume-like  
310 folds (e.g. over 800 m fold amplitude in Figure 1d). Our model is at a starting point of the large-  
311 scale folding formation. However, these folds are probably much older and can undergo multi-  
312 stage deformations during the long evolution of the ice sheet. Due to the density contrasts with  
313 cold ice above, the buoyancy of the warm ice below may also contribute to amplification of large-  
314 scale folds over long time scales. Our model size could be another limitation. The maximum  
315 strain is about 50% shortening in our bumpy bedrock models (e.g. Figures 3a-3e). The folds  
316 could be amplified more with an increasing strain but that would require a much larger model  
317 size (more computing time) to obtain a suitable fold wavelength. These problems are expected to  
318 be carefully tested and improved in future modeling.

## 319 **5 Conclusions**

320 Motivated by observations of folds in radargrams of the Greenland ice sheet, we  
321 conducted full-Stokes ice flow modeling with Underworld2 to reproduce large-scale englacial  
322 folds. Our modeling results show that: (1) Large-scale folds can form in convergent ice flow and  
323 are mainly controlled by rheological anisotropy of ice and bedrock topography, instead of  
324 vertical viscosity contrasts from temperature gradients in ice layers. (2) As observed in ice  
325 sheets, large-scale fold amplitudes are highest in the middle of the ice column and decrease  
326 towards the surface. Meanwhile, near-base fold patterns are more complex and often result in  
327 recumbent folds due to the bedrock constraint. (3) Ice anisotropy due to the CPO allows to  
328 produce small-scale folds on initially flat internal horizons. Finally, using movement tracking  
329 and strain analysis, our modeling helps to better understand ice-flow dynamics of the Greenland  
330 ice sheet. In particular, an improved implementation of ice anisotropy and basal shearing can  
331 result in high-strain-rate areas where the power-law ice would be softened, even on a frozen  
332 ground. This indicates that ice sheets could be more unstable when suddenly triggered to flow by  
333 external forcings, such as climate change, ice-sheet geometry changes or tectonic events.

## 334 **Acknowledgments**

335 Steven Franke was funded by the Walter Benjamin Programme of the German Research  
336 Foundation (Deutsche Forschungsgemeinschaft; DFG) – project number: 506043073, and Yu  
337 Zhang by the China Scholarship Council (grant no. 202006010063).

## 339 **Open Research**

340 Underworld is fully open-source and the version (v2.14.1b) used for this paper is available  
341 through Mansour et al. (2022) <https://doi.org/10.5281/zenodo.5935717>. Our code files for all the  
342 models are available through Zenodo <https://doi.org/10.5281/zenodo.10265944>. The radio-echo  
343 sounding data shown in Figure 1c (profile IDs: 20180509\_01\_[011, 012]) and in Figure 1f  
344 (profile ID: 20180512\_02\_009) from AWI's EGRIP-NOR-2018 survey are available under  
345 <https://doi.org/10.1594/PANGAEA.928569> (Franke et al., 2022b), the data shown in Figure 1d  
346 (profile ID: 20110507\_01\_032) is available via the CReSIS Data Products  
347 (<https://data.cresis.ku.edu/>) and the data shown in Figure 1e (profile ID: 20180415\_06\_007) is  
348 available under <https://doi.org/10.1594/PANGAEA.949391> (Franke et al., 2022a). Bed elevation  
349 data from Morlighem et al. (2017) and ice flow velocity data from Joughin et al. (2018) are

350 available at the National Snow and Ice Data Center: <https://nsidc.org/data/idbmg4> and  
351 <https://nsidc.org/data/nsidc-0670/>, respectively.

352

## 353 **References**

354 Artemieva, I. M. (2019). Lithosphere thermal thickness and geothermal heat flux in Greenland  
355 from a new thermal isostasy method. *Earth-Science Reviews*, 188, 469-481.

356 <https://doi.org/10.1016/j.earscirev.2018.10.015>

357 Bell, R. E., Tinto, K., Das, I., Wolovick, M., Chu, W., Creyts, T. T., et al. (2014). Deformation,  
358 warming and softening of Greenland's ice by refreezing meltwater. *Nature Geoscience*, 7(7),

359 497-502. <https://doi.org/10.1038/ngeo2179>

360 Beucher, R., Giordani, J., Moresi, L., Mansour, J., Kaluza, O., Velic, M., et al. (2022).

361 Underworld2: Python Geodynamics Modelling for Desktop, HPC and Cloud (v2.14.1b)

362 [Software]. Zenodo. <https://doi.org/10.5281/zenodo.7455999>

363 Biot, M. A. (1957). Folding instability of a layered viscoelastic medium under compression.

364 *Proceedings of the Royal Society of London. Series A. Mathematical and Physical Sciences*,

365 242(1231), 444-454. <https://doi.org/10.1098/rspa.1957.0187>

366 Bons, P. D., Jansen, D., Mundel, F., Bauer, C. C., Binder, T., Eisen, O., et al. (2016). Converging

367 flow and anisotropy cause large-scale folding in Greenland's ice sheet. *Nature communications*,

368 7(1), 11427. <https://doi.org/10.1038/ncomms11427>

369 Bons, P. D., Kleiner, T., Llorens, M. G., Prior, D. J., Sachau, T., Weikusat, I., & Jansen, D.

370 (2018). Greenland Ice Sheet: Higher nonlinearity of ice flow significantly reduces estimated

371 basal motion. *Geophysical Research Letters*, 45(13), 6542-6548.

372 <https://doi.org/10.1029/2018GL078356>

- 373 Duval, P., Ashby, M. F., & Anderman, I. (1983). Rate-controlling processes in the creep of  
374 polycrystalline ice. *The Journal of Physical Chemistry*, 87(21), 4066-4074.  
375 <https://doi.org/10.1021/j100244a014>
- 376 Franke, S., Bons, P. D., Westhoff, J., Weikusat, I., Binder, T., Streng, K., et al. (2022a).  
377 Holocene ice-stream shutdown and drainage basin reconfiguration in northeast Greenland.  
378 *Nature Geoscience*, 15(12), 995-1001. <https://doi.org/10.1038/s41561-022-01082-2>
- 379 Franke, S., Jansen, D., Binder, T., Paden, J. D., Dörr, N., Gerber, T. A., et al. (2022b). Airborne  
380 ultra-wideband radar sounding over the shear margins and along flow lines at the onset region of  
381 the Northeast Greenland Ice Stream. *Earth System Science Data*, 14(2), 763–779.  
382 <https://doi.org/10.5194/essd-14-763-2022>
- 383 Franke, S., Bons, P. D., Streng, K., Mundel, F., Binder, T., Weikusat, I., et al. (2023). Three-  
384 dimensional topology dataset of folded radar stratigraphy in northern Greenland. *Scientific Data*,  
385 10(1), 525. <https://doi.org/10.1038/s41597-023-02339-0>
- 386 Gillet-Chaulet, F., Gagliardini, O., Meyssonier, J., Montagnat, M., & Castelnau, O. (2005). A  
387 user-friendly anisotropic flow law for ice-sheet modeling. *Journal of Glaciology*, 51(172), 3-14.  
388 <https://doi.org/10.3189/172756505781829584>
- 389 Gillet-Chaulet, F., Gagliardini, O., Meyssonier, J., Zwinger, T., & Ruokolainen, J. (2006).  
390 Flow-induced anisotropy in polar ice and related ice-sheet flow modelling. *Journal of non-*  
391 *newtonian fluid mechanics*, 134(1-3), 33-43. <https://doi.org/10.1016/j.jnnfm.2005.11.005>
- 392 Glen, J. W. (1955). The creep of polycrystalline ice. Proceedings of the Royal Society of  
393 London. Series A. *Mathematical and Physical Sciences*, 228(1175), 519-538.  
394 <https://doi.org/10.1098/rspa.1955.0066>

- 395 Goldsby, D. L. (2006). Superplastic flow of ice relevant to glacier and ice-sheet mechanics.  
396 *Glacier science and environmental change*, 308-314.  
397 <https://doi.org/10.1002/9780470750636.ch60>
- 398 Hills, B. H., Harper, J. T., Humphrey, N. F., & Meierbachtol, T. W. (2017). Measured horizontal  
399 temperature gradients constrain heat transfer mechanisms in Greenland ice. *Geophysical*  
400 *Research Letters*, 44(19), 9778-9785. <https://doi.org/10.1002/2017GL074917>
- 401 Hudleston, P. J. (2015). Structures and fabrics in glacial ice: A review. *Journal of Structural*  
402 *Geology*, 81, 1-27. <https://doi.org/10.1016/j.jsg.2015.09.003>
- 403 Joughin, I. A. N., Smith, B. E., & Howat, I. M. (2018). A complete map of Greenland ice  
404 velocity derived from satellite data collected over 20 years. *Journal of Glaciology*, 64(243), 1-  
405 11. <https://doi.org/10.1017/jog.2017.73>
- 406 Krabbendam, M. (2016). Sliding of temperate basal ice on a rough, hard bed: creep mechanisms,  
407 pressure melting, and implications for ice streaming. *The Cryosphere*, 10(5), 1915-1932.  
408 <https://doi.org/10.5194/tc-10-1915-2016>
- 409 Kuiper, E. J. N., De Bresser, J. H., Drury, M. R., Eichler, J., Pennock, G. M., & Weikusat, I.  
410 (2020). Using a composite flow law to model deformation in the NEEM deep ice core,  
411 Greenland–Part 2: The role of grain size and premelting on ice deformation at high homologous  
412 temperature. *The Cryosphere*, 14(7), 2449-2467. <https://doi.org/10.5194/tc-14-2449-2020>
- 413 Leysinger Vieli, G. M., Martin, C., Hindmarsh, R. C. A., & Lüthi, M. P. (2018). Basal freeze-on  
414 generates complex ice-sheet stratigraphy. *Nature Communications*, 9(1), 4669.  
415 <https://doi.org/10.1038/s41467-018-07083-3>

- 416 Llorens, M. G., Bons, P. D., Griera, A., Gomez-Rivas, E., & Evans, L. A. (2013). Single layer  
417 folding in simple shear. *Journal of Structural Geology*, 50, 209-220.  
418 <https://doi.org/10.1016/j.jsg.2012.04.002>
- 419 Llorens, M. G., Griera, A., Steinbach, F., Bons, P. D., Gomez-Rivas, E., Jansen, D., et al. (2017).  
420 Dynamic recrystallization during deformation of polycrystalline ice: insights from numerical  
421 simulations. *Philosophical Transactions of the Royal Society A: Mathematical, Physical and*  
422 *Engineering Sciences*, 375(2086), 20150346. <https://doi.org/10.1098/rsta.2015.0346>
- 423 MacGregor, J. A., Fahnestock, M. A., Catania, G. A., Paden, J. D., Prasad Gogineni, S., Young,  
424 S. K., et al. (2015). Radiostratigraphy and age structure of the Greenland Ice Sheet. *Journal of*  
425 *Geophysical Research: Earth Surface*, 120(2), 212-241. <https://doi.org/10.1002/2014JF003215>
- 426 Marion, G. M., & Jakubowski, S. D. (2004). The compressibility of ice to 2.0 kbar. *Cold Regions*  
427 *Science and Technology*, 38(2-3), 211-218. <https://doi.org/10.1016/j.coldregions.2003.10.008>
- 428 Martín, C., Gudmundsson, G. H., Pritchard, H. D., & Gagliardini, O. (2009). On the effects of  
429 anisotropic rheology on ice flow, internal structure, and the age-depth relationship at ice divides.  
430 *Journal of Geophysical Research: Earth Surface*, 114(F4).  
431 <https://doi.org/10.1029/2008JF001204>
- 432 Moresi, L., & Mühlhaus, H. B. (2006). Anisotropic viscous models of large-deformation Mohr–  
433 Coulomb failure. *Philosophical Magazine*, 86(21-22), 3287-3305.  
434 <https://doi.org/10.1080/14786430500255419>
- 435 Moresi, L., Dufour, F., & Mühlhaus, H. B. (2003). A Lagrangian integration point finite element  
436 method for large deformation modeling of viscoelastic geomaterials. *Journal of computational*  
437 *physics*, 184(2), 476-497. [https://doi.org/10.1016/S0021-9991\(02\)00031-1](https://doi.org/10.1016/S0021-9991(02)00031-1)

438 Morlighem, M., Williams, C. N., Rignot, E., An, L., Arndt, J. E., Bamber, J. L., ... & Zinglensen,  
439 K. B. (2017). BedMachine v3: Complete bed topography and ocean bathymetry mapping of  
440 Greenland from multibeam echo sounding combined with mass conservation. *Geophysical*  
441 *research letters*, 44(21), 11-051. <https://doi.org/10.1002/2017GL074954>  
442 NEEM community members. (2013). Eemian interglacial reconstructed from a Greenland folded  
443 ice core. *Nature*, 493, 489–494. <https://doi.org/10.1038/nature11789>  
444 Pattyn, F., Perichon, L., Aschwanden, A., Breuer, B., De Smedt, B., Gagliardini, O., ... &  
445 Zwinger, T. (2008). Benchmark experiments for higher-order and full-Stokes ice sheet models  
446 (ISMIP–HOM). *The Cryosphere*, 2(2), 95-108. <https://doi.org/10.5194/tc-2-95-2008>  
447 Rogozhina, I., Martinec, Z., Hagedoorn, J. M., Thomas, M., & Fleming, K. (2011). On the long-  
448 term memory of the Greenland Ice Sheet. *Journal of Geophysical Research: Earth Surface*,  
449 116(F1). <https://doi.org/10.1029/2010JF001787>  
450 Sachau, T., Yang, H., Lang, J., Bons, P. D., & Moresi, L. (2022). ISMIP-HOM benchmark  
451 experiments using Underworld. *Geoscientific Model Development*, 15(23), 8749-8764.  
452 <https://doi.org/10.5194/gmd-15-8749-2022>  
453 Schmalholz, S. M., & Mancktelow, N. S. (2016). Folding and necking across the scales: a review  
454 of theoretical and experimental results and their applications. *Solid Earth*, 7(5), 1417-1465.  
455 <https://doi.org/10.5194/se-7-1417-2016>  
456 Sharples, W., Moresi, L. N., Velic, M., Jadamec, M. A., & May, D. A. (2016). Simulating faults  
457 and plate boundaries with a transversely isotropic plasticity model. *Physics of the Earth and*  
458 *Planetary Interiors*, 252, 77-90. <https://doi.org/10.1016/j.pepi.2015.11.007>

459 Wolovick, M. J., Creyts, T. T., Buck, W. R., & Bell, R. E. (2014). Traveling slippery patches  
460 produce thickness-scale folds in ice sheets. *Geophysical Research Letters*, 41(24), 8895-8901.

461 <https://doi.org/10.1002/2014GL062248>

462

463 **Reference From the Supporting Information**

464 Pettit, E. C., Waddington, E. D., Harrison, W. D., Thorsteinsson, T., Elsberg, D., Morack, J., &

465 Zumberge, M. A. (2011). The crossover stress, anisotropy and the ice flow law at Siple Dome,

466 West Antarctica. *Journal of Glaciology*, 57(201), 39-52.

467 <https://doi.org/10.3189/002214311795306619>